Optics & Laser Technology 179 (2024) 111273

Contents lists available at ScienceDirect

Optics and Laser Technology

journal homepage: www.elsevier.com/locate/optlastec

Full length article

Characterization of the polarization state of few-cycle laser pulses using d-scan: D-TURTLE

Óscar Pérez-Benito, Rosa Weigand *

Department of Optics, Faculty of Physics, Universidad Complutense de Madrid, Avda. Complutense s/n, 28040 Madrid, Spain

ARTICLE INFO

Keywords:
Ultrashort pulses
Polarization measurement
Spectral phase retrieval
Second harmonic generation
Femtosecond lasers
Temporal characterization of polarized pulses

ABSTRACT

We characterize the polarization state of few-femtosecond laser pulses by implementing the dispersion scan technique in combination with the tomographic ultrafast retrieval of transverse light E-fields procedure (D-TURTLE). We demonstrate, both numerically and experimentally, that D-TURTLE unambiguously identifies the pulse ellipticity, its handedness and which polarization component travels ahead. Given the robustness of this technique, and its self-referenced and in-line nature, D-TURTLE can be extremely useful to characterize polarized few-cycle laser pulses.

1. Introduction

Ultrashort polarized pulses are present in many physical systems and processes. In optomagnetic studies a variety of processes make use of polarized laser beams to understand the interaction of spins with light (magneto-optical Faraday, Kerr, Cotton-Mouton, Voigt effects) [1]. In high harmonic generation (HHG) the use of polarization-tailored pulses influences the interaction between the field and an atomic or solid system [2–4]. Ultrafast ellipsometry provides information about transient states of matter [5]. In other research fields polarization shaped pulses are used to coherently control a given physical process, including multiphoton ionization, optical control of lattice vibrations, coherent Raman scattering, or nano-optics [6].

Pioneering works [7,8] proposed the method tomographic ultrafast retrieval of transverse light E-fields (TURTLE) using SHG-FROG (second harmonic generation - frequency resolved optical gating) to temporally characterize polarized femtosecond pulses. TURTLE was suggested to be adequate with any characterization method which determines the amplitude and spectral phase of an ultrashort laser pulse. Different variants of this technique are DFG-XTURTLE (difference frequency generation cross-polarized TURTLE) which combines TURTLE with XFROG (cross-polarized FROG) to characterize polarized UV laser pulses of tens of femtoseconds [9] or V-FROG (single-scan vectorial FROG) which was used to characterize the polarization state of a ~ 40 fs pulse by rotating the polarization of the incoming pulse and recording a single SHG-FROG trace [10]. Other authors have employed d-scan (dispersion scan) with external polarizers to demonstrate the synthesis of a pulse which is linearly polarized in a time interval which is much shorter than the original duration of the pulses [11], which is an interesting configuration for HHG [12,13]. The recently developed A-swing technique [14] for the spectro-temporal characterization of ultrashort laser pulses has been extended to characterize pulses of several tens of femtoseconds with temporally varying polarizations [15]. Other techniques which involve Mach–Zehnder interferometers and known reference pulses have also been developed to spatio-temporally characterize the polarization state of vector pulses [16,17].

In this paper we adapt the TURTLE method to use it in combination with the d-scan technique for the characterization of ultra-broadband laser pulses with any polarization state. As a result we have an in-line, self-referenced technique which easily identifies the handedness of the field, lacks of temporal ambiguities, even when the polarization components do not overlap in time, and is specially suitable for few-cycle laser pulses.

2. Method

SHG-based d-scan makes use of a variable dispersion unit to generate phase-dependent SH spectra of ultra-broadband laser pulses from a single laser beam, displaying a d-scan trace. This trace is later processed to determine the electric field of a pulse in the time and in the spectral domain [18]. As in other techniques, the zero and first order terms of the phases, which account for the relative position of the maxima of the field oscillation with respect to the envelope, and for an absolute temporal delay of the field, respectively, cannot be determined. D-scan has successfully been employed for the spectro-temporal characterization of sub-2 cycles pulses from laser oscillators

* Corresponding author.
E-mail addresses: oscper03@ucm.es (Ó. Pérez-Benito), weigand@fis.ucm.es (R. Weigand).

https://doi.org/10.1016/j.optlastec.2024.111273
Received 24 October 2023; Received in revised form 20 May 2024; Accepted 4 June 2024
Available online 15 June 2024

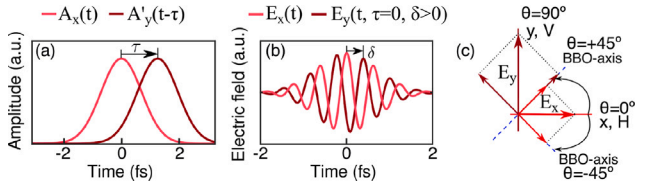

Fig. 1. Conventions employed. Field components of Eq. (2): $E_x(t)$ (red), $E_y(t)$ (dark red). (a) Temporal delay τ between envelopes $A_x(t)$ and $A_y(t)$; (b) Relative phase parameter δ. (c) Projections of $E_x(t)$ and $E_y(t)$ components on the BBO-axis for a given time t.

[19], pulses from laser amplifiers [20], and has been further developed to single-shot [21] or self-diffraction [22] configurations, or to employ alternative nonlinear materials such as nanoparticles [23]. A review with more implementations of d-scan can be found in [24]. All these previous works characterized linearly polarized laser pulses.

A polarized laser field propagating in the z direction can be described in the spectral domain through its field components $\tilde{E}_x(\omega)$ and $\tilde{E}_y(\omega)$. If $\tilde{I}_{x,y}(\omega)$, and $\varphi_{x,y}(\omega)$ are the spectra and spectral phases of $\tilde{E}_x(\omega)$ and $\tilde{E}_y(\omega)$ respectively, we derive the field amplitudes from the pulse spectrum as $\tilde{A}_{x,y}(\omega) = \sqrt{\tilde{I}_{x,y}(\omega)}$. The electric field components can be then expressed in the spectral and temporal domains, making use of the Fourier transform as:

$$\tilde{E}_x(\omega) = \tilde{A}_x(\omega)e^{i\varphi_x(\omega)} \overset{\mathcal{F}^{-1}}{\Longrightarrow} E_x(t) = A_x(t)e^{i\phi_x(t)}$$

$$\tilde{E}_y(\omega) = \tilde{A}_y(\omega)e^{i\varphi_y(\omega)} \overset{\mathcal{F}^{-1}}{\Longrightarrow} E_y(t) = A_y(t)e^{i\phi_y(t)} \quad (1)$$

In order to implement an efficient retrieval algorithm, we have to take into account two important facts. On one side the envelopes of the E_x and E_y components may have a relative temporal delay τ, and on the other side it is convenient to consider a possible relative phase parameter δ between the oscillation of each field component (Fig. 1(a), (b), notice that δ is not a carrier-envelope phase). Therefore we describe the field components as:

$$E_x(t) = A_x(t)e^{i\phi_x(t)}$$

$$E_y(t) = A'_y(t-\tau)e^{i(\phi'_y(t)-\delta)} = A_y(t)e^{i\phi_y(t)} \quad (2)$$

The underlying concept of D-TURTLE is to obtain SHG d-scan traces using a BBO crystal oriented at different rotation angles θ. We consider a coordinate system with reference to the plane of incidence on the BBO crystal: coordinate x (horizontal orientation) is contained in the plane of incidence, coordinate y (vertical orientation) is perpendicular to the plane of incidence, coordinate z is the propagation axis of the laser pulse, and the observer faces the light beam. We choose the BBO-axis set at $\theta = 0°$ when it generates the maximum SHG signal for horizontally polarized light. Positive and negative θ angles are measured with respect to this orientation (see Fig. 1(c)).

Let us now consider a polarized pulse. For a horizontally oriented BBO-axis the E_x component of the electric field will generate SH, while the E_y component will not. If the crystal is rotated, let us say to $\theta = +45°$, for a given time t the contribution of the E_x, E_y components to SH will be given by the interference of their projections on the BBO-axis. In the case of Fig. 1(c) both components have projections on the same side of the BBO-axis, and they constructively interfere. On the contrary, if the crystal is rotated to $\theta = -45°$ the projections of E_x and E_y have opposite directions and they destructively interfere. Therefore, the generated SH electric field will be different for both cases, as well as the d-scan traces. Notice that in the FROG implementations of TURTLE [7,8] a polarizer creates the interference field, which is then frequency-doubled in the BBO crystal, while in our implementation the BBO crystal assumes both roles.

We will now show, both numerically and experimentally, that a set of four d-scan traces generated with the BBO-axis oriented horizontally (H, $\theta = 0°$), vertically (V, $\theta = 90°$), at $\theta = -45°$ and at $\theta = +45°$ allows to temporally characterize the polarization state of an ultra-broadband few-cycle laser pulse.

3. Simulation results

We have run several simulations to check for the performance of D-TURTLE, prior to doing the measurements. The results can be found in Appendix A, as well as more detailed comments. First, we simulated D-TURTLE traces (at $\theta = 0°, 90°, \mp 45°$) generated by two components $E_x(t)$, $E_y(t)$, which were mathematically identical in amplitude and phase. To check whether the technique discriminates between clockwise and counter-clockwise rotation, and whether it identifies which component travels ahead, as seen by the observer, we applied three different pairs of values of parameter δ ($\pm\pi/4, \pm\pi/2, \pm 3\pi/4$) for three different delays τ (0, ±4 fs). The transform limited (TL) durations were 5.5 fs for both components. For $\tau = 0$ (Fig. A1.1) the results show that traces simulated for different values of $|\delta|$ are different, but very similar for $\pm\delta$ (column (a) Fig. A1.1). In column (b) shows the proposed pulse profiles for both components with their relative phase difference $\phi_y - \phi_x$ and total electric field. The handedness of the rotation can be specified since it is a numerical simulation. However column (c) shows that the difference between traces generated for $+\delta$ and $-\delta$ with the BBO crystal set $\theta = -45°$ and $\theta = +45°$ is negligible, in the order of magnitude of 10^{-16}. This hints for the fact that it would be very difficult to unambiguously retrieve the field and we can expect in this case that the technique does not discriminate between clockwise and counter-clockwise rotation. When $\tau \neq 0$ (Figs. A1.2–A1.4) the traces obtained for $+\delta$ and -δ are different, but traces obtained for a pair $(+\tau, +\delta)$ are identical to those obtained for the pair $(-\tau, -\delta)$. We can conclude that in the case of mathematically identical field components, the technique is ambiguous.

In real cases though, the components easily differ from each other, so we simulated cases in which the components have different field amplitudes (TL durations 5.5 fs for $|E_x|^2$ and 5.0 fs for $|E_y|^2$, Figs. A2.1–A2.4), or different phases (Figs. A3.1–A3.4). In both cases, for $\tau = 0$ (Figs. A2.1–A3.1) the results show that, unlike the case of Fig. A1.1, traces simulated for the same $|\delta|$ are sensitive to the sign of δ and therefore the technique discriminates between clockwise and counter-clockwise rotation. When $\tau \neq 0$ (Figs. A2.2–A2.4, A3.2–A3.4) the traces obtained for $+\delta$ and -δ are again different, and traces obtained for a pair $(+\tau, +\delta)$ and a pair $(-\tau, -\delta)$ are not equal. We can conclude that in realistic cases D-TURTLE can unambiguously identify the relative temporal state of E_y with respect to E_x and therefore the polarization state of the pulse.

Furthermore, when both components do not overlap in time (example for $\tau = \pm 200$ fs is given in Appendix A, Fig. A4) the presence of spectral interference fringes reveal that the field components are temporally far apart. The traces obtained at $\theta = -45°$ for $\tau = +200$ fs or $\tau = -200$ fs are different when the components are not mathematically equivalent. The same happens for $\theta = +45°$. This renders the technique as sensitive to discriminate in realistic cases which polarization component travels ahead.

These conclusions have also been checked by retrieving all cases in Figs. A1, A2, A3 and A4. The retrieval algorithm is based on a standard d-scan retrieval technique combined with the description of the field components given in Eq. (2) (Details in Appendix B).

The results of the simulations and their subsequent retrievals demonstrate the capability of D-TURTLE to determine the value and sign of the relative phase $(\phi_y - \phi_x)$ between field components. It can also ascertain whether the E_x component precedes the E_y component or vice versa. In summary, the D-TURTLE technique provides a complete characterization of the polarization state along the few-cycle pulse and is capable of unambiguously determining which component travels ahead, even when they do not overlap in time.

In the following section, some experimental cases are proposed and tested.

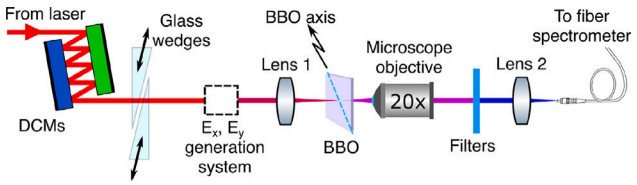

Fig. 2. Experimental set-up. See text for details.

4. Experimental results

We employed a house-made Ti:Sa oscillator which delivers few-cycle ultra-broadband horizontally polarized pulses, centered at 762 nm, at 76 MHz repetition rate with an average power of 50 mW. To perform d-scan, a set of DCMs (Double-Chirped Mirrors, Venteon DCM7, six pairs of bounces) and a pair of BK7 wedges were used. To generate field components E_x, E_y, we placed different systems at the exit of the compressor. The output pulse is focused using a lens (Lens 1, f = 1 cm) onto a commercially available type-I 10 μm thick BBO crystal for SHG (cut at 29.2°), which can be oriented at any angle θ (see Fig. 1(c)). The SHG signal is collected using a 20× microscope objective and filtered (Schott filters BG40 (2×) and BG23) prior to being focused with a fused-silica lens (Lens 2, f = 5 cm) onto a UV solarized optical fiber (400 μm nucleus diameter) coupled to a UV spectrometer (Ocean Optics, HR4000). The time required to obtain a full set of D-TURTLE traces in our configuration is around 15 min, since each d-scan measurement takes around 2-3 min when accumulating the spectrum signal during 10 ms for each insertion step. Notice that the choice of a lens with a 1 cm focal length is not determining, and longer focal lengths can also be used, as in any SHG based temporal characterization technique.

Aditionally, with the aid of a linear polarizer, the average power for each component was measured (Thorlabs, S121C power sensor), as well as the transmitted linear spectrum (Ocean Optics, USB4000). The algorithm is fed with this information, in order to avoid unnecessary uncertainties, which could affect the performance of the retrieval procedure. Details about the retrieval algorithm are given in Appendix B. The set-up used is depicted in Fig. 2.

4.1. Quarter-wave plate

The first system was an ultra-broadband quarter-wave plate (Venteon, 600–950 nm) oriented at $\alpha = +45°$ ($\alpha = 0°$ means fast axis horizontally oriented), which should produce clockwise rotating circularly polarized light (Fig. 3, column A), or at $\alpha = -45°$ to produce counter-clockwise rotating circularly polarized light (Fig. 3, column B). In Fig. 3, column A, the traces for θ=0° and θ=90° are not identical, due to subtle differences in the amplitudes and/or spectral phases of the components. The differences are also present in the cases $\theta = \mp 45°$. Due to these slight asymmetries, the retrieval algorithm easily identifies the synthesis of an almost circularly polarized pulse rotating clockwise, as expected for a quarter-wave plate oriented at $\alpha = +45°$, providing a $\phi_y - \phi_x$ value close to $+\pi/2$. In Fig. 3, column B, the appearance of the traces obtained for the different angles θ is at first sight similar to case A. However the retrieval algorithm perfectly identifies a different value for the relative phase $\phi_y - \phi_x$, being in this case close to $-\pi/2$, i.e. a counter-clockwise rotating field, as expected for a quarter-wave plate oriented at $\alpha = -45°$.

Note that the quarter-wave plate employed guarantees a $\pi/2$ dephasing only between 600 and 950 nm (while the linear spectrum of the laser reaches the 1000 nm zone) and this may contribute to the fact that the retrieved relative temporal phases are not exactly $\pm\pi/2$ in Fig. 3 (A11) and (B11), respectively. The durations for $|E_x|^2$ and $|E_y|^2$ were 6.9 fs in both cases.

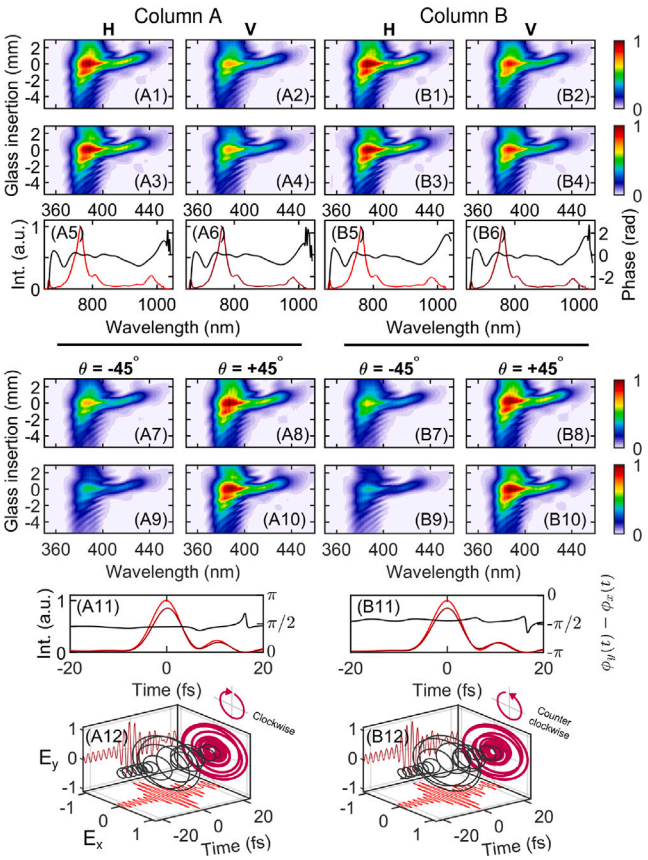

Fig. 3. Quarter-wave plate at $\alpha = \pm 45°$ (column A, B). Numbers: 1, 2 experimental traces with BBO crystal at $\theta = 0°$, $\theta = 90°$; 3, 4 corresponding retrieved traces; 5, 6 spectra and spectral phases for components E_x (red) and E_y (dark red); 7, 8 experimental traces with BBO crystal at $\theta = \mp 45°$; 9, 10 corresponding retrieved traces; 11 pulses and relative temporal phase $\phi_y - \phi_x$; 12 total field.

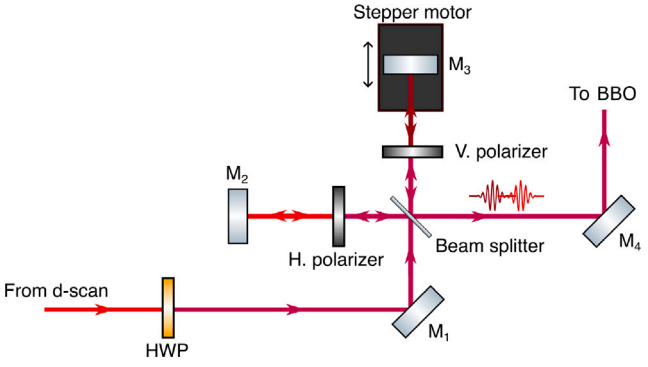

Fig. 4. Scheme of the Michelson interferometer. HWP: Halfwave plate at $\alpha = +22.5°$. M_1–M_4: Silver mirrors.

4.2. Non-overlapping polarization components

The second system was a Michelson interferometer and the specific set-up can be seen in Fig. 4. The colors of the beams are meant to identify the horizontal (red) and vertical (dark red) components, as well as the total field (fuchsia).

To generate the E_x and E_y components an ultra-broadband half-wave plate (Venteon, 600–950 nm) was set at $\alpha = +22.5°$ to produce linearly polarized light at +45° and it was placed at the entrance of the interferometer. To select E_x and E_y components a wire-grid polarizer (Thorlabs, WP25M-UB) was set in each arm of the interferometer.

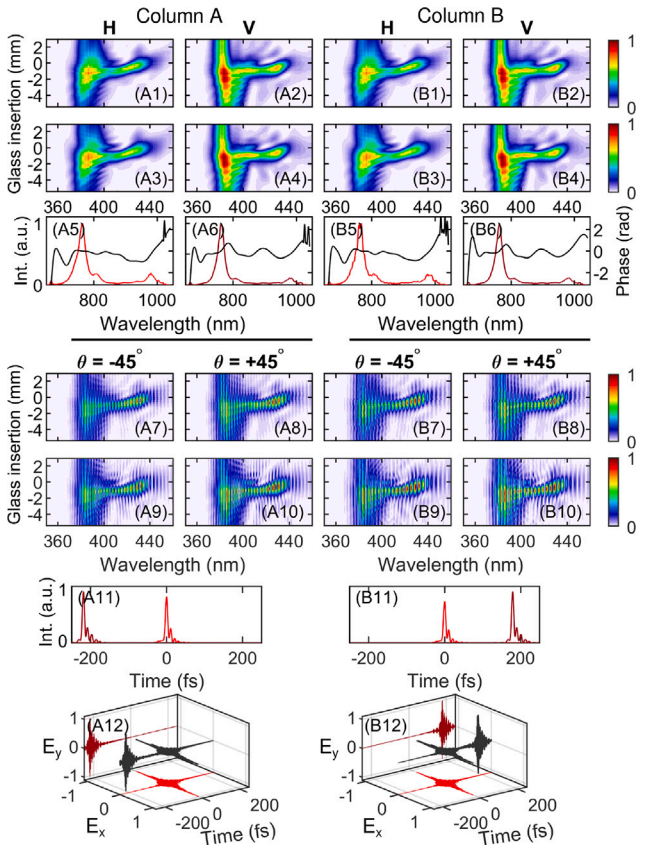

Fig. 5. H, V components with relative delay $\tau \simeq \mp$ 200 fs (column A, B). Numbers: 1, 2 experimental traces with BBO crystal at $\theta = 0°$, $\theta = 90°$; 3, 4 corresponding retrieved traces; 5, 6 spectra and spectral phases for components E_x (red) and E_y (dark red); 7, 8 experimental traces with BBO crystal at $\theta = \mp 45°$; 9, 10 corresponding retrieved traces; 11 pulses and relative temporal phase $\phi_y - \phi_x$; 12 total field.

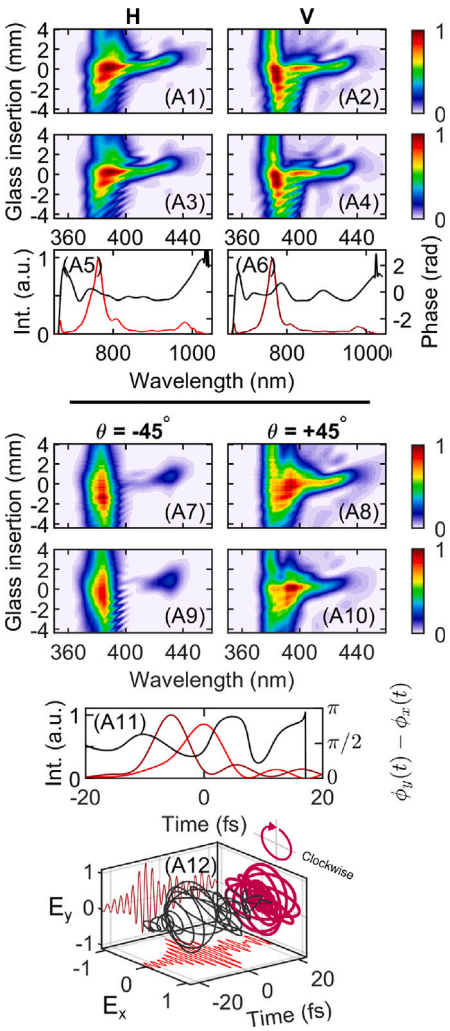

Fig. 6. General field with E_x and E_y having different spectra and spectral phases and a temporal delay $\tau \simeq -5.5$ fs. (A1), (A2): Experimental traces with BBO crystal at $\theta = 0°$, $\theta = 90°$; (A3), (A4): corresponding retrieved traces; (A5), (A6): spectra and spectral phases for components E_x (red) and E_y (dark red); (A7), (A8): experimental traces with BBO crystal at $\theta = \mp 45°$; (A9), (A10) corresponding retrieved traces; (A11) pulses and relative temporal phase $\phi_y - \phi_x$; (A12) total field.

The temporal delay τ was set by placing the mirror in arm E_y on a motorized stage. In a case where both components do not overlap in time ($\tau \simeq \mp 200$ fs, Fig. 5 columns A, B) spectral interference leaves its imprint in the d-scan traces, so a first inspection reveals whether the pulse polarization components are disassembled. Moreover the retrieval finds the correct solution and, in spite of having temporally separated pulses, there is no ambiguity and D-TURTLE can identify which component travels ahead. The durations for $|E_x|^2$ and $|E_y|^2$ were 8.2 fs and 6.9 fs respectively.

4.3. Partially overlapped polarization components

Let us recall that each arm of the Michelson interferometer provides E_x and E_y components which have different spectral characteristics, as it can be seen in the spectra and spectral phases of Fig. 5 A5/A6 or B5/B6. We took advantage of this fact to synthesize a polarized pulse with a temporally changing ellipticity and, for generality, we added a temporal delay between the components which was close to, but different to optical contact.

The results can be seen in (Fig. 6). The technique perfectly identifies that the E_y component travels 5.5 fs ahead of the E_x component (hence τ=−5.5 fs). Along the pulse, the phase difference (Fig. 6 A11) ranges from $+\pi/4$ to $+\pi$ approximately. This causes significant changes in the ellipticity of the field, while the handedness of the rotation is always clockwise. This rich behavior can be observed in Fig. 6 A12.

4.4. Anisotropic polyimide film

Once the performance of the technique was proven in systems where the expected results were known, we tested another system consisting of a thin polyimide film (Kapton), which is an anisotropic medium with well-defined perpendicularly oriented axes (identified by placing the film between two crossed polarizers) and unknown birefringence. The film was set at $\alpha = +45°$ with respect to one of its axes, (Fig. 7, column A) or at $\alpha = -45°$ (Fig. 7, column B). For both cases A and B, the experimental measurements clearly show that the horizontal and vertical components are different in spectrum and intensity (notice that H-traces are weaker than V-traces and their intensity have been artificially increased 10 times to represent them in the same false-color scale than the rest of the traces). With this information, qualitatively obtained by a first analysis of the experimental measurements (prior to any retrieval), one can suspect that the total fields are elliptically polarized and elongated in the vertical axis. The retrieval procedure finds total fields that agree with this observation and also identifies a change in the handedness of the rotation of the field depending on the angle chosen ($\alpha = +45°$ or $\alpha = -45°$). This is also a consistent behavior, since the Kapton film has well-defined perpendicularly oriented axes. In these cases the phase difference is close to $\pm\pi/2$ and the durations for $|E_x|^2$ and $|E_y|^2$ were 6.9 fs and 7.1 fs respectively.

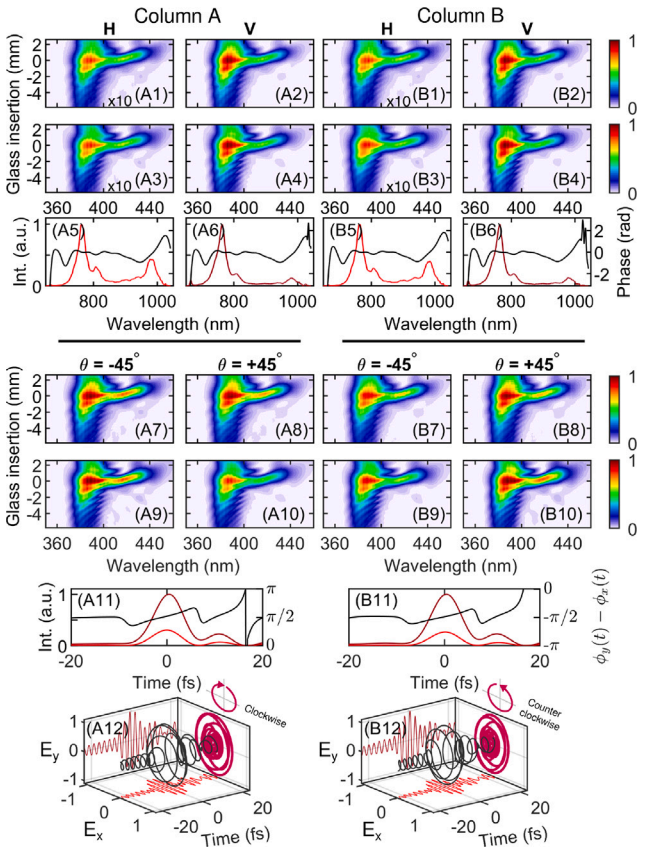

Fig. 7. Thin polyimide film (Kapton) with an axis at $\alpha = +45°$ (column A), Kapton with the same axis at $\alpha = -45°$ (column B). Numbers: 1, 2 experimental traces with BBO crystal at $\theta = 0°$, $\theta = 90°$; 3, 4 corresponding retrieved traces; 5, 6 spectra and spectral phases for components E_x (red) and E_y (dark red); 7, 8 experimental traces with BBO crystal at $\theta = \mp 45°$; 9, 10 corresponding retrieved traces; 11 pulses and relative temporal phase $\phi_y - \phi_x$; 12 total field.

5. Discussion

The extension of the d-scan technique to characterize few-cycle polarized pulses has been successfully implemented and its generality proven. D-scan has an inline geometry, it uses a single beam and this characteristic has been preserved in the implementation performed.

A first insight using an approach based on numerical simulations revealed that, as long as the polarization components of the total field are not mathematically identical, d-scan traces taken at four different orientation angles of a SHG-crystal, are qualitatively and quantitatively different enough to perform a full spectro-temporal characterization of both polarization components. The retrieval algorithm that we have developed for that purpose is based on a standard d-scan algorithm, however we have extended it to properly handle the relative temporal delay and phase between components. This extension includes the use of the minimization of two different error functions, that allow to unambiguously characterize the polarization state of arbitrarily polarized few-cycle laser pulses. Moreover, the technique has been demonstrated to be self-referenced, i.e. no additional technique is needed to spectro-temporally characterize the polarized field.

The experimental results obtained in different systems corroborate that a set of four d-scan measurements, along with an algorithm perfectly identifies the spectro-temporal characteristics of each polarization component as well as their relative temporal position, even in cases where the components do not overlap in time. In this way the total field is therefore fully characterized and the ellipticity of the field and the handedness of the polarization vector rotation properly determined along the time axis.

6. Conclusions

The simulations and retrievals of both the experimental measurements and the simulations shown in this work render D-TURTLE as a robust in-line and self-referenced technique to directly and unambiguously determine ellipticity, handedness and the relative temporal position between components of few-cycle polarized pulses.

CRediT authorship contribution statement

Óscar Pérez-Benito: Conceptualization, Data curation, Formal analysis, Investigation, Methodology, Software, Validation, Visualization, Writing – original draft, Writing – review & editing. **Rosa Weigand:** Conceptualization, Formal analysis, Funding acquisition, Investigation, Methodology, Project administration, Resources, Software, Supervision, Validation, Writing – original draft, Writing – review & editing.

Declaration of competing interest

The authors declare that they have no known competing financial interests or personal relationships that could have appeared to influence the work reported in this paper.

Data availability

Data will be made available on request.

Acknowledgments

R. Weigand thanks MICINN/AEI for funding the project PID2022-136260NB-I00. O. Pérez-Benito acknowledges a predoctoral contract from UCM (call CT63/19-CT64/19).

Appendix A. Details on simulation results

To check for the performance of the D-TURTLE technique (d-scan in combination with TURTLE) three sets of simulations were run. The first one represents a case in which the field components E_x and E_y are mathematically identical in spectrum and spectral phase, while the other two cases simulate more realistic scenarios in which the components E_x and E_y are slightly different in spectrum or spectral phase.

In Figs. A1 to A4, we provide the field components used for the simulations in the spectral and temporal domains, the simulated D-TURTLE traces (i.e. the set of d-scan traces obtained for $\theta = 0°, 90°, -45°, +45°$) for different values of τ and δ, the three-dimensional view of the total field and the difference between traces for either different values $+\delta$ and $-\delta$, or different values of pairs $(+\tau, +\delta)$ and $(-\tau, -\delta)$, or different values $+\tau$ and $-\tau$.

Figs. A1.1, A1.2, A1.3 and A1.4 show the D-TURTLE traces obtained for E_x, E_y components with the same field amplitudes (Gaussian shape in frequencies), spectral phases zero (therefore Transform Limited pulses) with the same time duration (5.5 fs) for different values of δ ($\pm\pi/4$, $\pm\pi/2$, $\pm 3\pi/4$), and for three different relative delays: $\tau = 0$ fs (Fig. A1.1), −4 fs (Fig. A1.2) and +4 fs (Fig. A1.3). For the case of perfectly overlapped components (τ=0 fs), simulations performed with the same absolute value of δ give identical traces when measured with the BBO crystal at $\theta = \mp 45°$. The difference between traces obtained for a $+\delta$ and a $-\delta$ value are shown in the right column (c) and in this case it has a negligible value ($\sim 10^{-16}$). On the other hand, for relative delays $\tau \neq 0$ fs (Figs. A1.2, $\tau = -4$ fs and A1.3, $\tau = +4$ fs), for a fixed value of τ the traces generated for $\pm\delta$ are different with the BBO crystal at $\theta = -45°$ (difference between traces ~ 0.5, right column). The same occurs for $\theta = +45°$. In these cases this allows to determine the handedness of the polarization state if the value of τ is known (Figs. A1.2 and A1.3). However, since the components are mathematically indistinguishable,

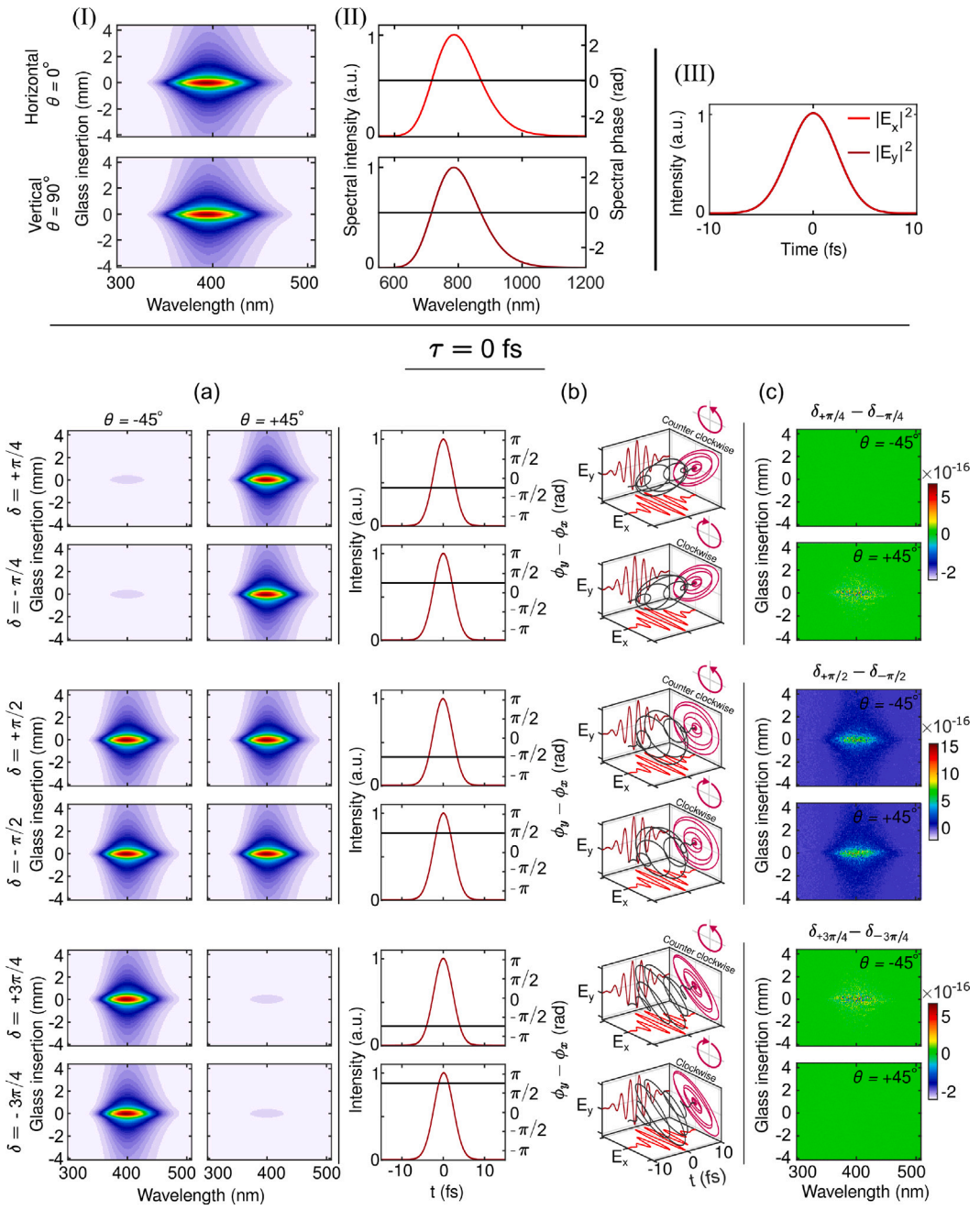

Fig. A1.1. Simulation for identical E_x and E_y components. E_x and E_y have the same field amplitudes (Gaussian shape in frequencies), spectral phases zero (i.e. Transform Limited pulses) with the same time duration (5.5 fs). The relative delay between components is $\tau = 0$ fs. Top panel: (I) Simulated traces for E_x and E_y with BBO crystal at $\theta = 0°$ and $\theta = 90°$, respectively. (II) Proposed spectra and spectral phases for E_x and E_y. (III) Proposed pulse profiles for E_x and E_y. Bottom panel: (a) Simulated traces with the BBO crystal set at $\theta = \mp 45°$ for different couples $\pm\delta$. (b) Proposed pulse profiles for both components with their relative phase difference $\phi_y - \phi_x$ and total electric field in 3D view. (c) Difference between traces generated for $+\delta$ and $-\delta$ with the BBO crystal set at $\theta = -45°$ and $\theta = +45°$.

there are degenerated cases. This is, the traces for the BBO crystal at $\theta = -45°$ are identical for the pairs of values $(+\tau, +\delta)$ and $(-\tau, -\delta)$ with negligible differences of $\sim 10^{-15}$ (Fig. A1.4). The same applies for the traces with the BBO crystal at $\theta = +45°$. These results show that, for mathematically identical components, the technique cannot obtain the value of τ and δ simultaneously and hence, it is not possible to know which component travels ahead of the other and the handedness of the rotation.

Figs. A2.1, A2.2, A2.3 and A2.4 show the traces obtained for E_x, E_y components with field amplitudes with Gaussian shape in frequencies, spectral phases zero (therefore Transform Limited pulses) with different time durations (5.5 fs for E_x and 5 fs for E_y) for different values of δ ($\pm\pi/4$, $\pm\pi/2$, $\pm 3\pi/4$) and for three different relative delays: $\tau = 0$ fs (Fig. A2.1), −4 fs (Fig. A2.2) and +4 fs (Fig. A2.3). As in the previous case, the traces obtained with the BBO crystal at $\theta = \mp 45°$ change for different absolute values of δ. However in this case, the technique shows differences between traces obtained with the BBO crystal at $\theta = -45°$ or $\theta = +45°$ depending on the sign of δ. This happens for all the τ values considered ($\sim 10^{-2}$ for τ=0 fs and ~ 0.5 for $\tau = \mp 4$ fs, Figs. A2.1–A2.3). In addition, since in this case the field components are distinguishable, there are no degenerate cases and traces generated by pairs of values $(+\tau, +\delta)$ and $(-\tau, -\delta)$ are not equivalent and show

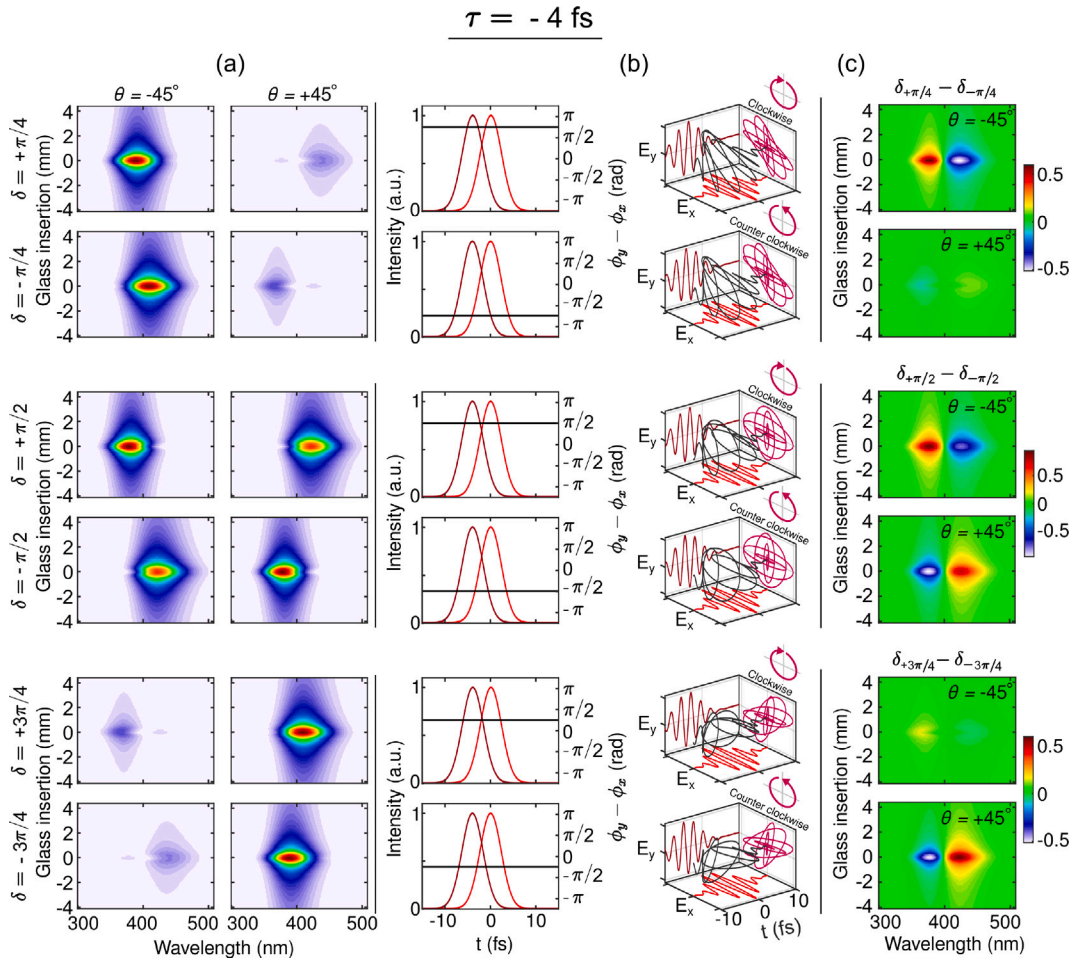

Fig. A1.2. Simulation with the same E_x and E_y components than A1.1 with a relative delay between components $\tau = -4$ fs. (a) Simulated traces with the BBO crystal set at $\theta = \mp 45°$ for different couples $\pm\delta$. (b) Proposed pulse profiles for both components with their relative phase difference $\phi_y - \phi_x$ and total electric field in 3D view. (c) Difference between traces generated for $+\delta$ and $-\delta$ with the BBO crystal set at $\theta = -45°$ and $\theta = +45°$.

differences of the order of $\sim 10^{-2}$ for both orientations of the BBO crystal at $\theta = -45°$ and $\theta = +45°$ (Fig. A2.4).

Figs. A3.1–A3.3 show the traces obtained for E_x, E_y components with field amplitudes with Gaussian shape in frequencies but different spectral phases for different values of δ ($\pm\pi/4$, $\pm\pi/2$, $\pm 3\pi/4$) and for three different relative delays: $\tau = 0$ fs (Fig. A3.1), -4 fs (Fig. A3.2) and $+4$ fs (Fig. A3.3). E_x, E_y components have the same field amplitudes (Gaussian shape in frequencies) but different spectral phases. The E_x component is Transform Limited (FWHM = 5.5 fs, spectral phase 0), while for the E_y component we depart from the settings of E_x and add a quadratic spectral phase. As in the previous case, different values of δ generate different traces for any value of τ, being in this situation even more noticeable with differences ranging from 10^{-2} to 0.2 (right columns, (c)). Again, the technique distinguishes between traces obtained with the BBO crystal at $\theta = -45°$ or $\theta = +45°$ for pairs of values $(+\tau, +\delta)$ and $(-\tau, -\delta)$ with differences of ~ 0.2, showing that there are no degenerate cases (Fig. A3.4).

This set of simulations clearly shows that the relative intensity of the traces at $\theta = -45°$ and $\theta = +45°$ determines the ellipticity of the total field, while the sign of the phase difference $\phi_y - \phi_x$ accounts for the handedness of the rotation. It also shows that the D-TURTLE technique is capable of unambiguously determine the relative delay and phase difference of two components, as long as they are not mathematically identical.

To further check for the robustness of the technique, we simulated components completely separated in time ($\tau = \pm 200$ fs) in order to know whether the method can identify which component travels ahead. The simulations have been done for the same three different cases shown above. Case 1: two mathematically identical E_x and E_y components with the same field amplitudes (Gaussian shape in frequencies), spectral phases zero (therefore Transform Limited pulses) with the same time duration (5.5 fs). Case 2: E_x, E_y components with field amplitudes with Gaussian shape in frequencies, spectral phases zero (therefore Transform Limited pulses) with different time durations (5.5 fs for E_x and 5 fs for E_y). Case 3: E_x, E_y components with field amplitudes Gaussian shape in frequencies (FWHM=5.5 fs) but different spectral phases. The E_x component is Transform Limited (spectral phase 0) while a quadratic spectral phase has been added to the E_y component.

Fig. A4 shows the traces generated by E_x and E_y with a relative delay of $\tau = \pm 200$ fs for the BBO crystal at angles $\theta = \mp 45$ (column a), the relative position of the components and the total field in 3D view (column b), and the difference between traces for $\tau = +200$ fs and $\tau = -200$ fs for angles of the BBO crystal $\theta = \mp 45$ (column c) for the three cases.

For case 1, the difference between traces for $\tau = +200$ fs and $\tau = -200$ fs is negligible (around $\sim 10^{-7}$) and therefore is not possible to distinguish which component arrives earlier.

For cases 2 and 3, the differences between traces for $\tau = +200$ fs and $\tau = -200$ fs, are in the order of $\sim 10^{-2}$ and $\sim 10^{-1}$ respectively. This

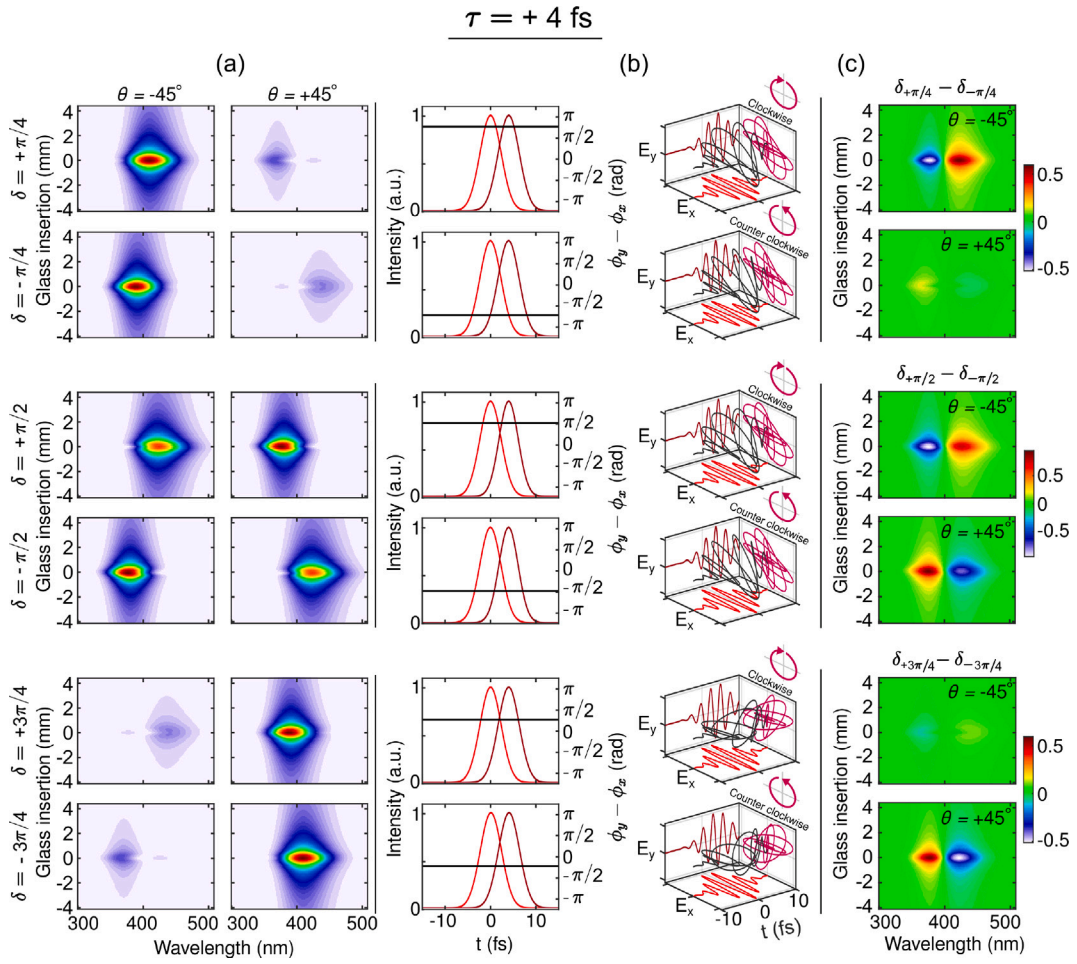

Fig. A1.3. Simulation with the same E_x and E_y components than A1.1 with a relative delay between components $\tau = +4$ fs. (a) Simulated traces with the BBO crystal set at $\theta = \mp 45°$ for different couples $\pm\delta$. (b) Proposed pulse profiles for both components with their relative phase difference $\phi_y - \phi_x$ and total electric field in 3D view. (c) Difference between traces generated for $+\delta$ and $-\delta$ with the BBO crystal set at $\theta = -45°$ and $\theta = +45°$.

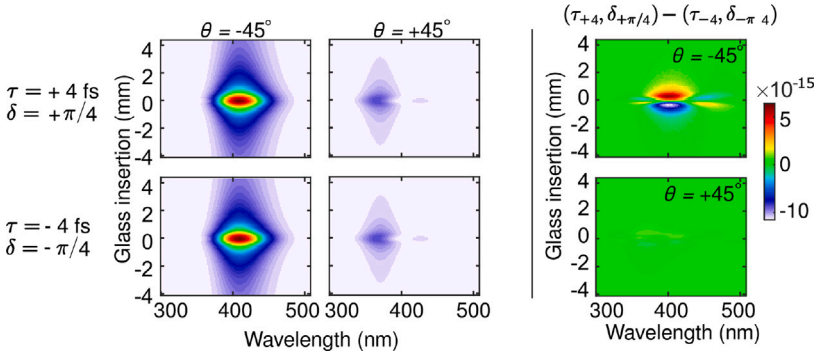

Fig. A1.4. Difference between simulated traces with the same E_x and E_y components of A1.1 for pairs of relative delays and phase parameters ($\tau = +4$ fs, $\delta = +\pi/4$) and ($\tau = -4$ fs, $\delta = -\pi/4$).

means that for these cases in which the components are not identical, the technique is capable to determine which component is ahead even, when they are completely separated in time.

Appendix B. τ–δ Retrieval algorithm

The retrieval process is run in two steps. First, the traces measured for the horizontal ($\theta = 0°$) and vertical ($\theta = 90°$) orientations of the BBO crystal are retrieved with a standard d-scan retrieval algorithm [18,19,23]. The linear spectrum of each component is measured behind a linear polarizer and is supplied to the algorithm. After both retrievals, also the spectral phases ϕ_x, ϕ_y of each component are known. Note that since, as other techniques, d-scan is insensitive to the zero and first-order terms of the spectral phase, the retrieved fields have absolute phase-shift zero (i.e. the maximum of the oscillation of the carrier coincides with the maximum of the field envelope) and there

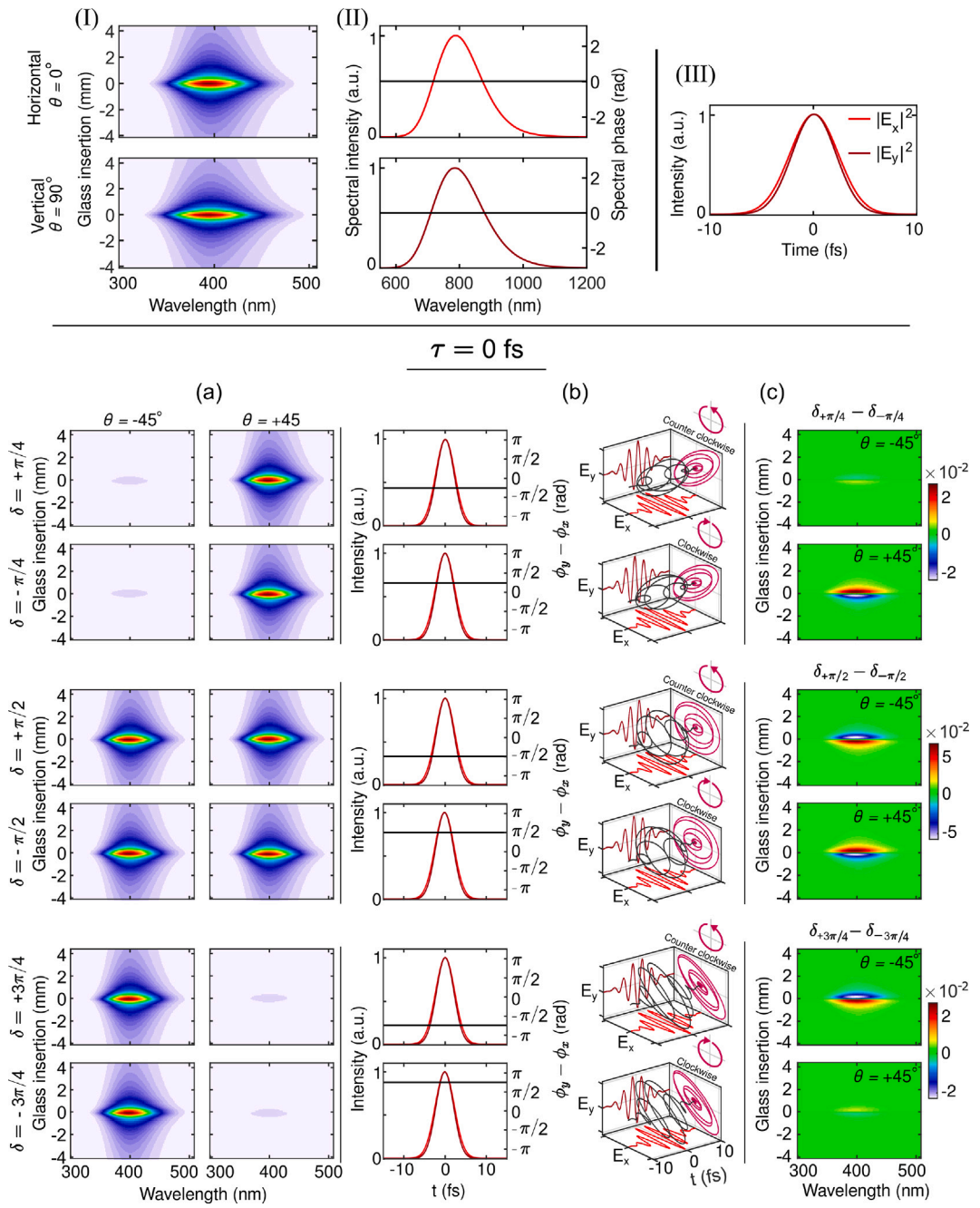

Fig. A2.1. Simulation for different E_x and E_y components. E_x and E_y components have field amplitudes with Gaussian shape in frequencies, spectral phases zero (i.e. Transform Limited pulses) with different time durations (5.5 fs for E_x and 5 fs for E_y). The relative delay between components is $\tau = 0$ fs. Top panel: (I) Simulated traces for E_x and E_y with BBO crystal at $\theta = 0°$ and $\theta = 90°$, respectively. (II) Proposed spectra and spectral phases for E_x and E_y. (III) Proposed pulse profiles for E_x and E_y. Bottom panel: (a) Simulated traces with the BBO crystal set at $\theta = \mp 45°$ for different couples $\pm\delta$. (b) Proposed pulse profiles for both components with their relative phase difference $\phi_y - \phi_x$ and total electric field in 3D view. (c) Difference between traces generated for $+\delta$ and $-\delta$ with the BBO crystal set at $\theta = -45°$ and $\theta = +45°$.

is no shift in time (the maximum of the field envelope occurs for $t = 0$ fs). In the second step, these two spectra and spectral phases, the relative power (as measured with a power meter after a linear polarizer) of both components, along with the traces measured with the BBO crystal at $\theta = -45°$ and $\theta = +45°$ are used to feed a retrieval algorithm (we call it τ-δ retrieval algorithm) which iteratively applies different values of τ and δ to the vertical component (see Eq. (2) of the manuscript) to simultaneously optimize the traces at $\theta = \mp 45°$. Values for τ are set typically in a range from −5 to 5 fs in steps of 0.1 fs for components which overlap in time, and −250 to 250 fs in steps of 1 fs for components which are completely separated in time. Values for δ are set in a range from $-\pi$ to π rad, typically in steps of $\pi/16$ rad. Notice that for each value of τ the full range of values for δ is scanned. These ranges need to be adjusted depending on the case under study, reaching a compromise between precision and computational time.

In each step of the loop, i.e. for each pair of (τ, δ) values, two traces for the BBO crystal at $\theta = -45°$ and $\theta = +45°$ are simulated. Then to find the optimal (τ, δ) values, the error analysis is done using two different error functions that jointly evaluate the similarity between the experimental and the simulated traces. The first error function evaluates how similar are the shapes of the simulated traces with respect to their corresponding experimental ones without taking into account the intensity ratio between traces at $\theta = -45°$ and $\theta = +45°$.

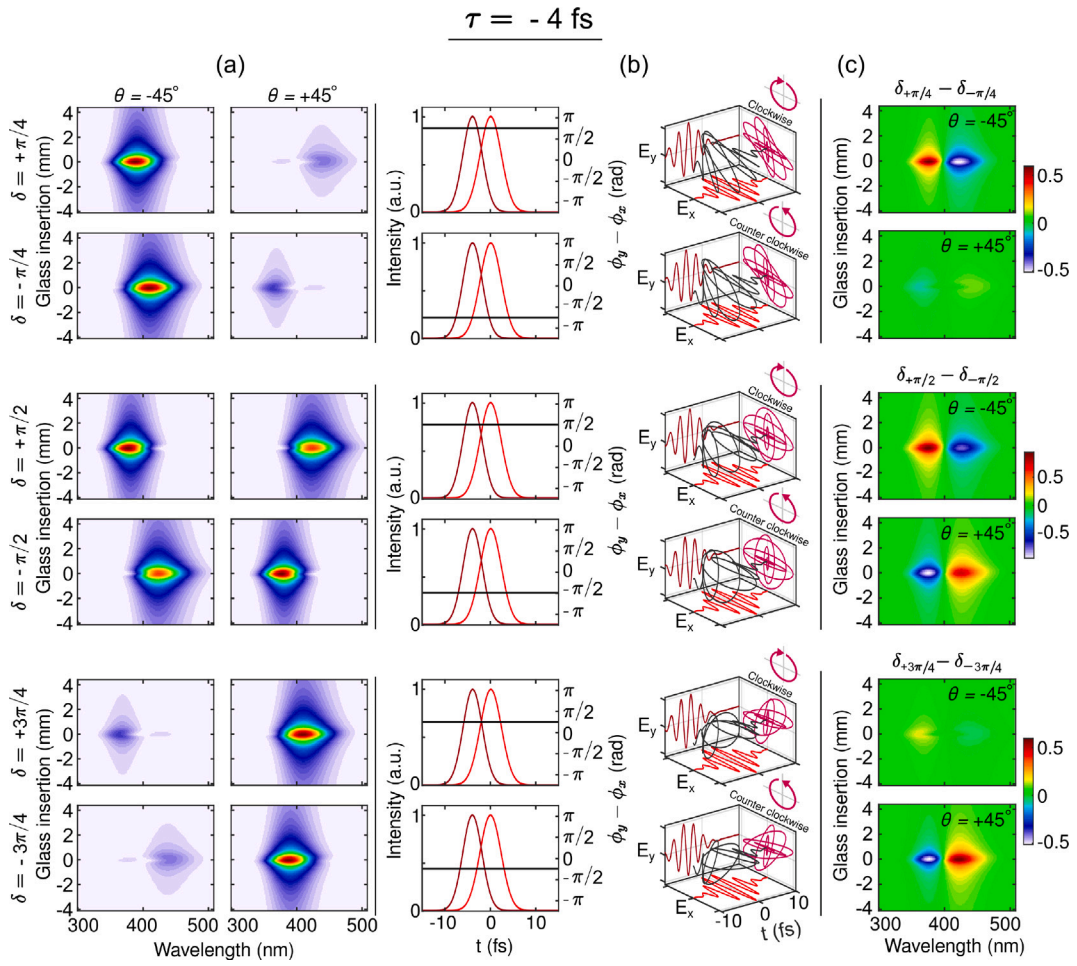

Fig. A2.2. Simulation with the same E_x and E_y components than A2.1 with a relative delay between components $\tau = -4$ fs. (a) Simulated traces with the BBO crystal set at $\theta = \mp 45°$ for different couples $\pm\delta$. (b) Proposed pulse profiles for both components with their relative phase difference $\phi_y - \phi_x$ and total electric field in 3D view. (c) Difference between traces generated for $+\delta$ and $-\delta$ with the BBO crystal set at $\theta = -45°$ and $\theta = +45°$.

This is calculated as follows:

$$G = \sqrt{\frac{\left(G_{\theta=-45°}\right)^2 + \left(G_{\theta=+45°}\right)^2}{2}}, \tag{B.1}$$

where the individual error of each trace is independently calculated as in the standard d-scan algorithm [19,23]:

$$G_{\theta=\mp 45°} = \sqrt{\frac{1}{N_\omega N_z}\sum_{i,j}^{N_\omega,N_z}\left(\hat{S}_{\mathrm{meas},\theta=\mp 45°}(\omega_i,z_j) - \hat{S}_{\mathrm{sim},\theta=\mp 45°}(\omega_i,z_j)\right)^2}. \tag{B.2}$$

$\hat{S}_{\mathrm{meas},\theta=\mp 45°}$ are the measured traces with the BBO crystal at $\theta = -45°$ or $\theta = +45°$, normalized their own maximum, $\hat{S}_{\mathrm{sim},\theta=\mp 45°}$ are the simulated traces with the BBO crystal at $\theta = -45°$ or $\theta = +45°$, normalized to their own maximum for that pair of (τ, δ) values, N_ω is the number of points in the frequency axis and N_z is the number of points in the dispersion axis.

On the contrary, the second error function just evaluates the difference in the intensity ratio of the simulated traces at $\theta = -45°$ and $\theta = +45°$ with respect to the corresponding intensity ratio of the experimental traces. Let us define $\hat{\hat{S}}_{\mathrm{meas},\theta=\mp 45°}(\omega, z)$ as the measured trace $S_{\mathrm{meas},\theta=\mp 45°}(\omega, z)$ normalized to the maximum between them both, i.e. $\max[\max(S_{\mathrm{meas},\theta=-45°}(\omega, z)), \max(S_{\mathrm{meas},\theta=+45°}(\omega, z))]$. And let us also define $\hat{\hat{S}}_{\mathrm{sim},\theta=\mp 45°}(\omega, z)$ as the simulated trace $S_{\mathrm{sim},\theta=\mp 45°}(\omega, z)$ normalized to the maximum between them both, i.e. $\max[\max(S_{\mathrm{sim},\theta=-45°}(\omega, z)), \max(S_{\mathrm{sim},\theta=+45°}(\omega, z))]$.

We can then calculate the error function R as follows:

$$R = \sqrt{\frac{(\mathrm{diff}_{\theta=-45°})^2 + (\mathrm{diff}_{\theta=+45°})^2}{2}} \tag{B.3}$$

where $\mathrm{diff}_{\theta=\mp 45°} = \frac{1}{N_\omega N_z}\left(\sum_{i,j}^{N_\omega,N_z}\hat{\hat{S}}_{\mathrm{meas},\theta=\mp 45°}(\omega_i,z_j) - \sum_{i,j}^{N_\omega,N_z}\hat{\hat{S}}_{\mathrm{sim},\theta=\mp 45°}(\omega_i,z_j)\right)$.

The final result for the pair of (τ, δ) values is chosen in such a way that optimizes both error functions G and R simultaneously, thus achieving retrieved traces which present shapes very similar to those measured and keep the same intensity ratio between traces (at $\theta = -45°$ and $\theta = +45°$) that is experimentally obtained. These definitions of G and R lead to error values between 0 and 1. The values obtained for good retrievals of D-TURTLE traces are of the same order of magnitude than those obtained for standard d-scan retrievals ($\sim 10^{-2}$). The use of two different error functions to obtain the relative state between the polarization components resulted to be crucial to unambiguously characterize all the polarization states presented in this work, including the handedness of the rotation of the polarization vector.

This algorithm has been tested by retrieving all the cases simulated in this document. In all cases, with the exception of the unrealistic case of mathematically identical components, the retrieved values of τ and δ were the same as the ones set in the simulation with a maximum error of 1 step ($|\Delta\tau| = 0.1$ fs and $|\Delta\delta| = \pi/16$ rad).

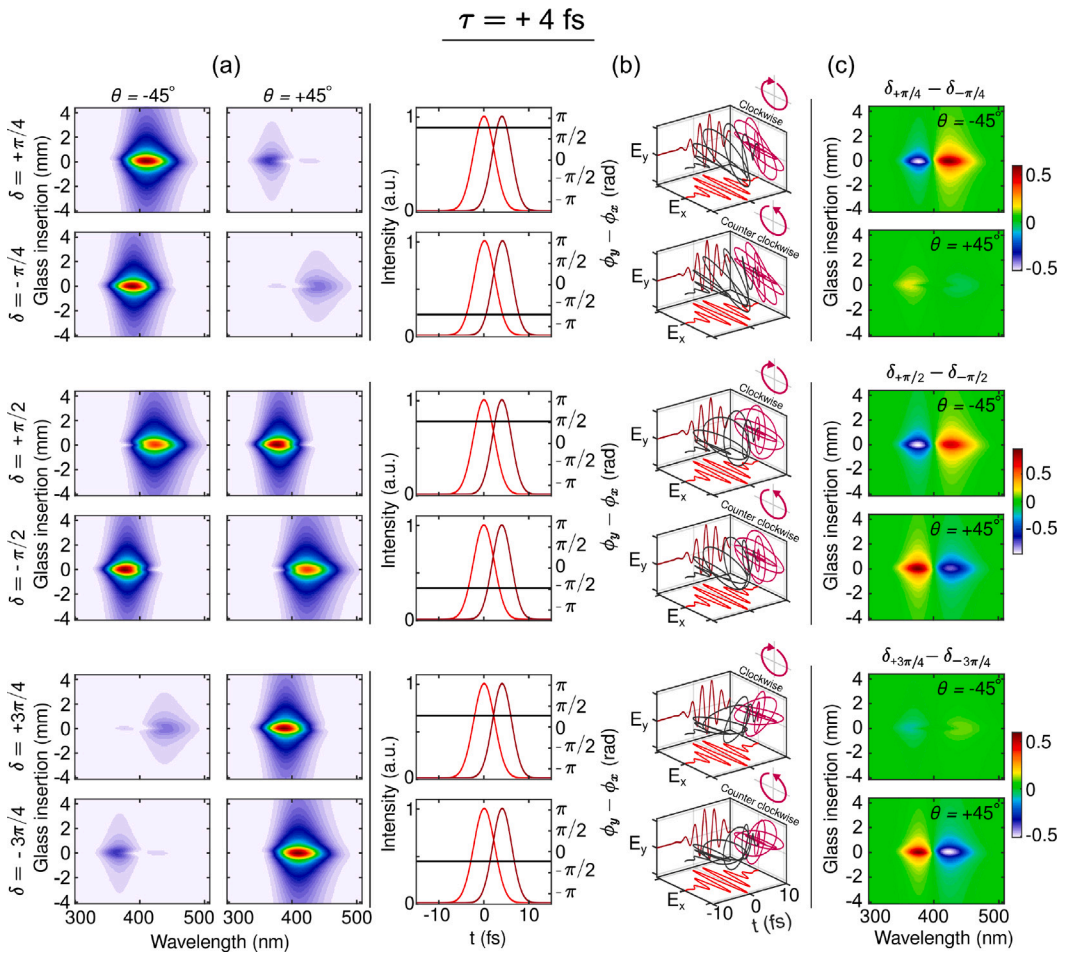

Fig. A2.3. Simulation with the same E_x and E_y components than A2.1 with a relative delay between components $\tau = +4$ fs. (a) Simulated traces with the BBO crystal set at $\theta = \mp 45°$ for different couples $\pm\delta$. (b) Proposed pulse profiles for both components with their relative phase difference $\phi_y - \phi_x$ and total electric field in 3D view. (c) Difference between traces generated for $+\delta$ and $-\delta$ with the BBO crystal set at $\theta = -45°$ and $\theta = +45°$.

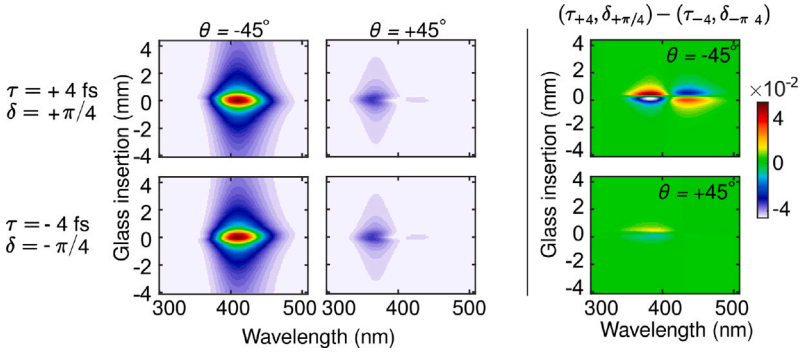

Fig. A2.4. Difference between simulated traces with the same E_x and E_y components of A2.1 with pairs of relative delays and phase parameters ($\tau = +4$ fs, $\delta = +\pi/4$) and ($\tau = -4$ fs, $\delta = -\pi/4$).

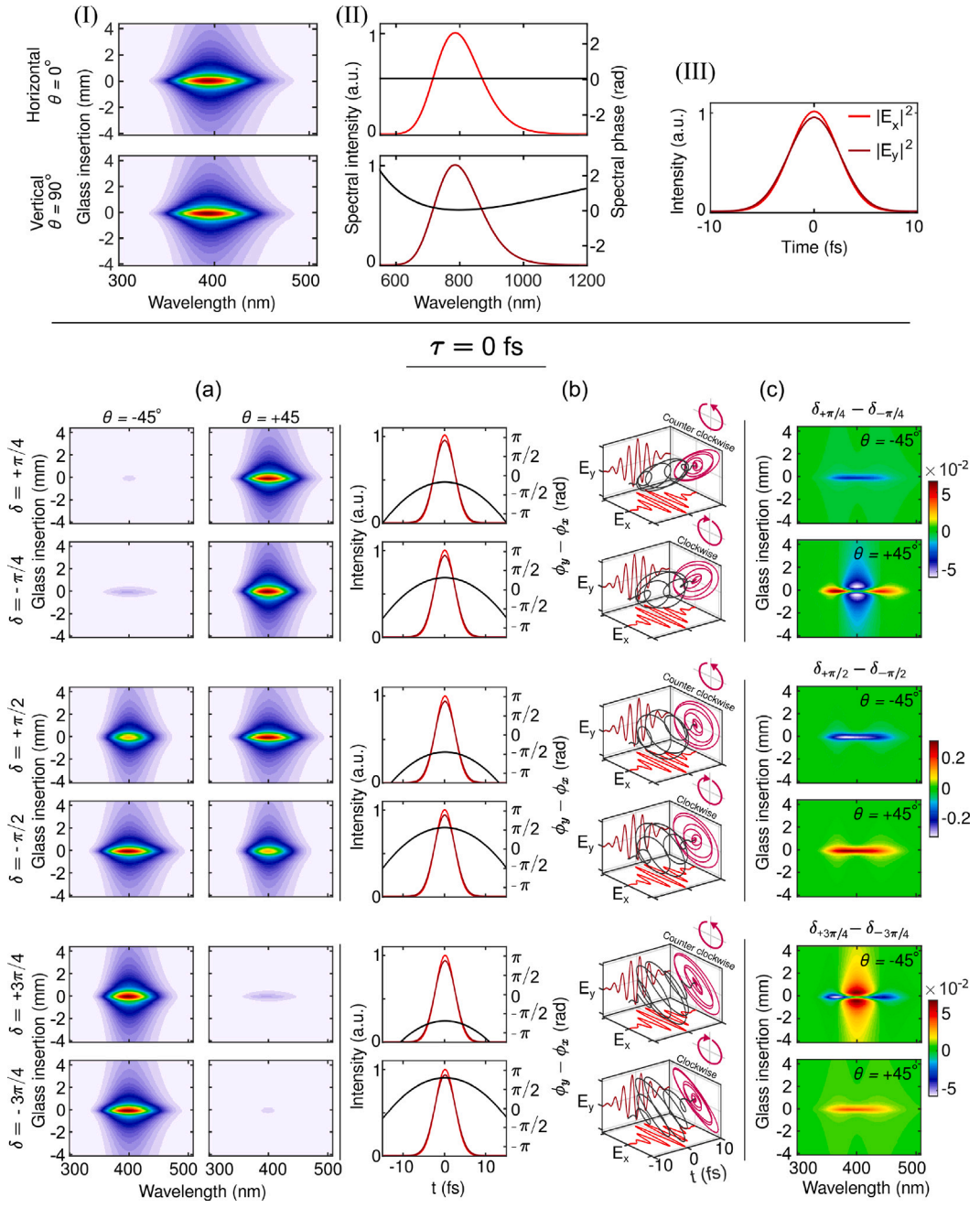

Fig. A3.1. Simulation for different E_x and E_y components. The E_x component is Transform Limited (FWHM = 5.5 fs, spectral phase 0), while for the E_y component we depart from the settings of E_x and add a quadratic spectral phase. The relative delay between components is $\tau = 0$ fs. Top panel: (I) Simulated traces for E_x and E_y with BBO crystal at $\theta = 0°$ and $\theta = 90°$, respectively. (II) Proposed spectra and spectral phases for E_x and E_y. (III) Proposed pulse profiles for E_x and E_y. Bottom panel: (a) Simulated traces with the BBO crystal set at $\theta = \mp 45°$ for different couples $\pm\delta$. (b) Proposed pulse profiles for both components with their relative phase difference $\phi_y - \phi_x$ and total electric field in 3D view. (c) Difference between traces generated for $+\delta$ and $-\delta$ with the BBO crystal set at $\theta = -45°$ and $\theta = +45°$.

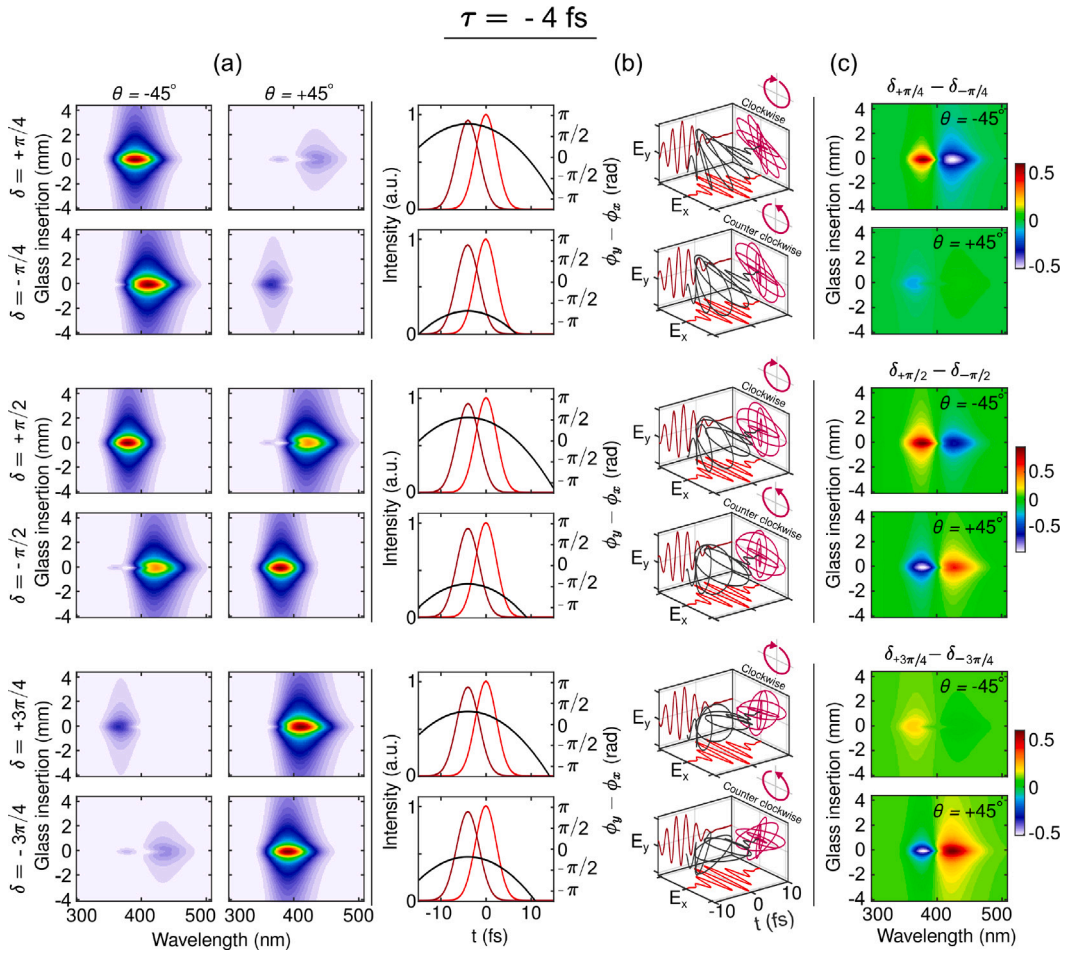

Fig. A3.2. Simulation with the same E_x and E_y components than A3.1 with a relative delay between components $\tau = -4$ fs. (a) Simulated traces with the BBO crystal set at $\theta = \mp 45°$ for different couples $\pm\delta$. (b) Proposed pulse profiles for both components with their relative phase difference $\phi_y - \phi_x$ and total electric field in 3D view. (c) Difference between traces generated for $+\delta$ and $-\delta$ with the BBO crystal set at $\theta = -45°$ and $\theta = +45°$.

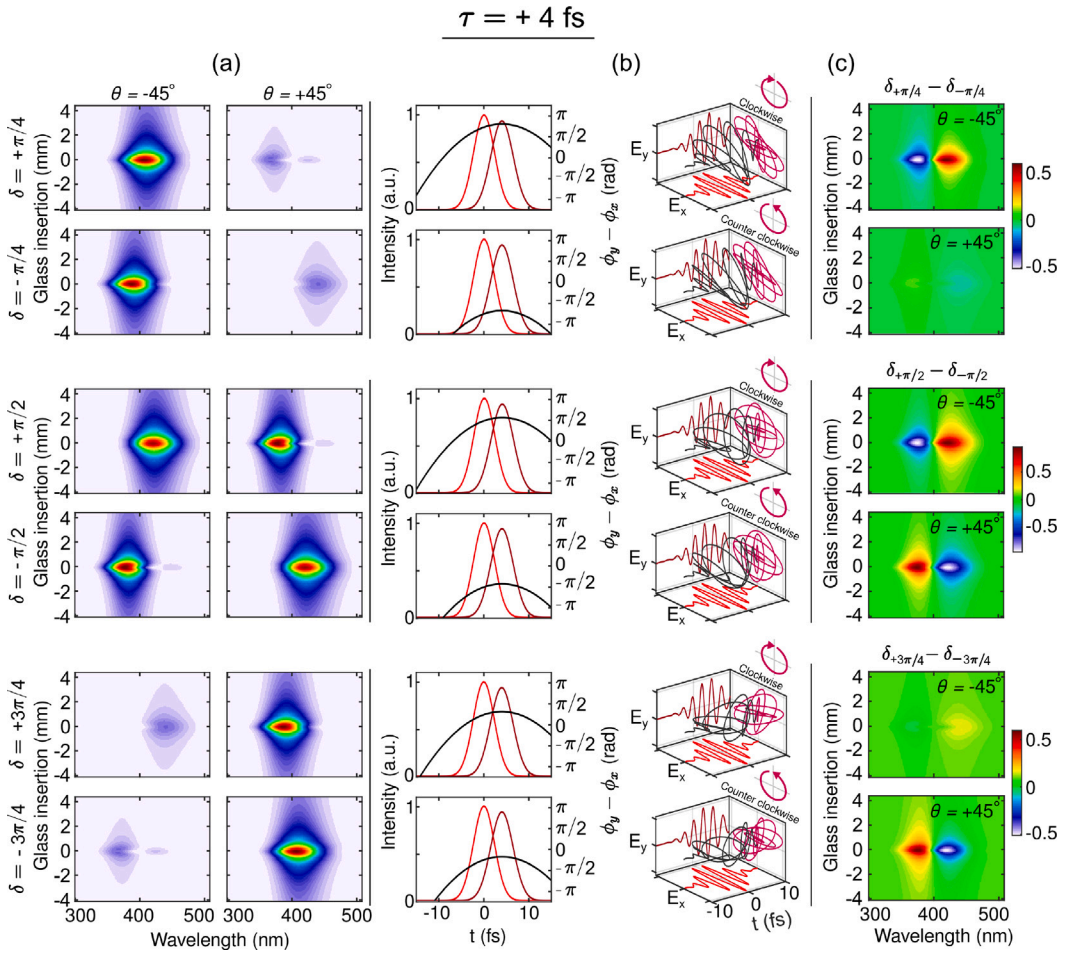

Fig. A3.3. Simulation with the same E_x and E_y components than A3.1 with a relative delay between components $\tau = +4$ fs. (a) Simulated traces with the BBO crystal set at $\theta = \mp 45°$ for different couples $\pm\delta$. (b) Proposed pulse profiles for both components with their relative phase difference $\phi_y - \phi_x$ and total electric field in 3D view. (c) Difference between traces generated for $+\delta$ and $-\delta$ with the BBO crystal set at $\theta = -45°$ and $\theta = +45°$.

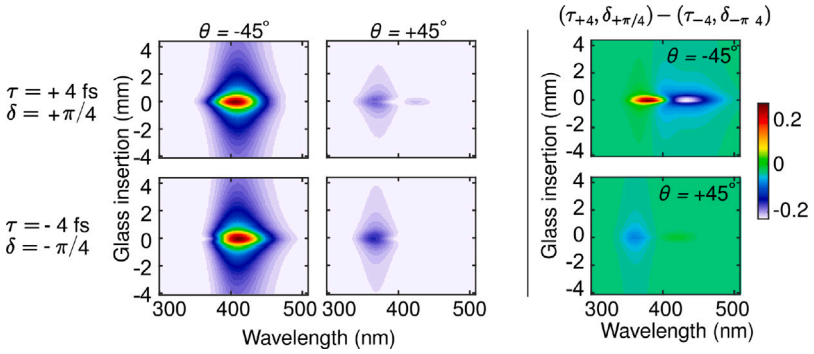

Fig. A3.4. Difference between simulated traces with the same E_x and E_y components of A3.1 with pairs of relative delays and phase parameters ($\tau = +4$ fs, $\delta = +\pi/4$) and ($\tau = -4$ fs, $\delta = -\pi/4$).

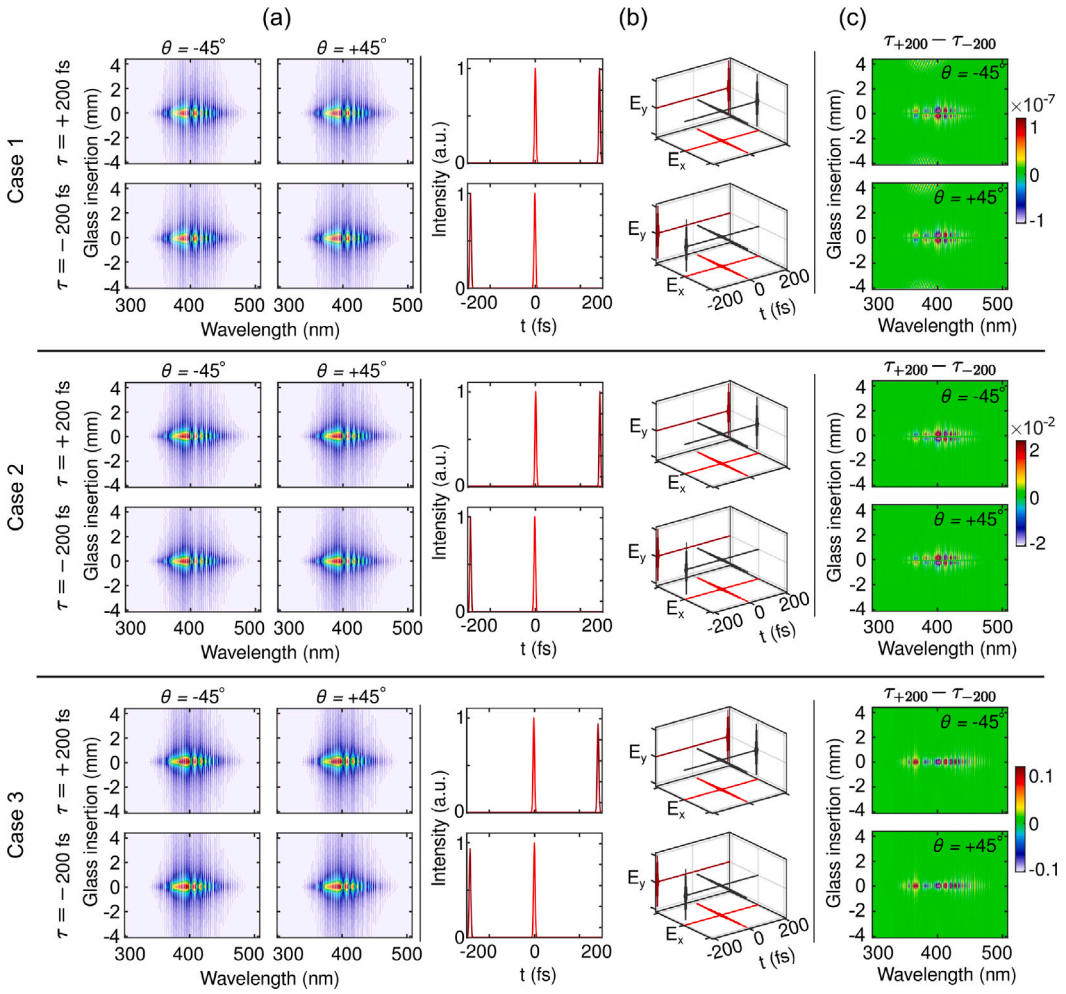

Fig. A4. Simulations for E_x and E_y components with a relative delay $\tau = \pm 200$ fs and δ=0 for three different cases. Case 1: E_x and E_y components of Fig. A1.1. Case 2: E_x and E_y components of Fig. A2.1. Case 3: E_x and E_y components of Fig. A3.1. (a) Simulated traces with the BBO crystal set at $\theta = \mp 45°$ for different couples $\pm\delta$. (b) Proposed pulse profiles for both components and total electric field in 3D view. (c) Difference between traces generated for $\tau = \pm 200$ fs with the BBO crystal set at $\theta = -45°$ and $\theta = +45°$.

References

[1] D. Bossini, V.I. Belotelov, A.K. Zvezdin, A.N. Kalish, A.V. Kimel, Magnetoplasmonics and femtosecond optomagnetism at the nanoscale, ACS Photon. 3 (8) (2016) 1385–1400, http://dx.doi.org/10.1021/acsphotonics.6b00107.

[2] J. Kasza, I. Magashegyi, P. Dombi, P. Földi, Polarization dependence of atomic high-order harmonic generation: Description using a discrete basis, Phys. Rev. A 105 (2022) 033105, http://dx.doi.org/10.1103/PhysRevA.105.033105.

[3] N. Klemke, N. Tancogne-Dejean, G.M. Rossi, Y. Yang, F. Scheiba, R. Mainz, G. Di Sciacca, A. Rubio, F. Kärtner, O. Mücke, Polarization-state-resolved high-harmonic spectroscopy of solids, Nature Commun. 10 (1) (2019) 1319, http://dx.doi.org/10.1038/s41467-019-09328-1.

[4] T. Heinrich, M. Taucer, O. Kfir, P. Corkum, A. Staudte, C. Ropers, M. Sivis, Chiral high-harmonic generation and spectroscopy on solid surfaces using polarization-tailored strong fields, Nature Commun. 12 (1) (2021) 3723, http://dx.doi.org/10.1038/s41467-021-23999-9.

[5] S. Richter, M. Rebarz, O. Herrfurth, S. Espinoza, R. Schmidt-Grund, J. Andreasson, Broadband femtosecond spectroscopic ellipsometry, Rev. Sci. Instrum. 92 (3) (2021) 033104, http://dx.doi.org/10.1063/5.0027219.

[6] K. Misawa, Applications of polarization-shaped femtosecond laser pulses, Adv. Phys.: X 1 (4) (2016) 544–569, http://dx.doi.org/10.1080/23746149.2016.1221327.

[7] P. Schlup, O. Masihzadeh, L. Xu, R. Trebino, R.A. Bartels, Tomographic retrieval of the polarization state of an ultrafast laser pulse, Opt. Lett. 33 (3) (2008) 267–269, http://dx.doi.org/10.1364/OL.33.000267.

[8] L. Xu, P. Schlup, O. Masihzadeh, R.A. Bartels, R. Trebino, Analysis of the measurement of polarization-shaped ultrashort laser pulses by tomographic ultrafast retrieval of transverse light E fields, J. Opt. Soc. Am. B 26 (12) (2009) 2363–2369, http://dx.doi.org/10.1364/JOSAB.26.002363.

[9] M.T. Seidel, Z. Zhang, S. Yan, K.L. Wells, H.-S. Tan, Characterization of polarization shaped ultraviolet femtosecond laser pulses, J. Opt. Soc. Am. B 28 (11) (2011) 2718–2725, http://dx.doi.org/10.1364/JOSAB.28.002718.

[10] G.I. Haham, A. Levin, P. Sidorenko, G. Lerner, O. Cohen, V-FROG—single-scan vectorial FROG, J. Phys. Photon. 3 (3) (2021) 034017, http://dx.doi.org/10.1088/2515-7647/ac0541.

[11] D.D. Rivas, A.-K. Raab, C. Guo, A.-L. Viotti, I. Sytcevich, A. L'Huillier, C. Arnold, Measurement of ultrashort laser pulses with a time-dependent polarization state using the d-scan technique, J. Phys.: Photon. 6 (1) (2024) 015003, http://dx.doi.org/10.1088/2515-7647/ad1c6c.

[12] R. López-Martens, J. Mauritsson, P. Johnsson, A. L'Huillier, O. Tcherbakoff, A. Zaïr, E. Mével, E. Constant, Time-resolved ellipticity gating of high-order harmonic emission, Phys. Rev. A 69 (2004) 053811, http://dx.doi.org/10.1103/PhysRevA.69.053811.

[13] I.J. Sola, A. Zaïr, R. López-Martens, P. Johnsson, K. Varjú, E. Cormier, J. Mauritsson, A. L'Huillier, V. Strelkov, E. Mével, E. Constant, Temporal and spectral studies of high-order harmonics generated by polarization-modulated infrared fields, Phys. Rev. A 74 (2006) 013810, http://dx.doi.org/10.1103/PhysRevA.74.013810.

[14] B. Alonso, W. Holgado, Í.J. Sola, Compact in-line temporal measurement of laser pulses with amplitude swing, Opt. Express 28 (10) (2020) 15625–15640, http://dx.doi.org/10.1364/OE.386321.

[15] C. Barbero, B. Alonso, Í.J. Sola, Characterization of ultrashort vector pulses from a single amplitude swing measurement, Opt. Express 32 (7) (2024) 10862–10873, http://dx.doi.org/10.1364/OE.515198.

[16] B. Alonso, I. Lopez-Quintas, W. Holgado, R. Drevinskas, P.G. Kazansky, C. Hernández-García, Í.J. Sola, Complete spatiotemporal and polarization characterization of ultrafast vector beams, Commun. Phys. 3 (1) (2020) http://dx.doi.org/10.1038/s42005-020-00419-w.

[17] A. Zdagkas, V. Nalla, N. Papasimakis, N.I. Zheludev, Spatio-temporal characterization of ultrashort vector pulses, APL Photon. 6 (11) (2021) 116103, http://dx.doi.org/10.1063/5.0056066.

[18] M. Miranda, T. Fordell, C. Arnold, A. L'Huillier, H. Crespo, Simultaneous compression and characterization of ultrashort laser pulses using chirped mirrors

and glass wedges, Opt. Express 20 (1) (2012) 688–697, http://dx.doi.org/10.1364/OE.20.000688.

[19] M. Miranda, C.L. Arnold, T. Fordell, F. Silva, B. Alonso, R. Weigand, A. L'Huillier, H. Crespo, Characterization of broadband few-cycle laser pulses with the d-scan technique, Opt. Express 20 (17) (2012) 18732–18743, http://dx.doi.org/10.1364/OE.20.018732.

[20] B. Alonso, I.J. Sola, H. Crespo, Self-calibrating d-scan: Measuring ultrashort laser pulses on-target using an arbitrary pulse compressor, Sci. Rep. 8 (2018) 3264, http://dx.doi.org/10.1038/s41598-018-21701-6.

[21] F.J. Salgado-Remacha, B. Alonso, H. Crespo, C. Cojocaru, J. Trull, R. Romero, M. López-Ripa, P.T. Guerreiro, F. Silva, M. Miranda, A. L'Huillier, C.L. Arnold, Í.J. Sola, Single-shot d-scan technique for ultrashort laser pulse characterization using transverse second-harmonic generation in random nonlinear crystals, Opt. Lett. 45 (14) (2020) 3925–3928, http://dx.doi.org/10.1364/OL.397033.

[22] M. Canhota, F. Silva, R. Weigand, H.M. Crespo, Inline self-diffraction dispersion-scan of over octave-spanning pulses in the single-cycle regime, Opt. Lett. 42 (15) (2017) 3048–3051, http://dx.doi.org/10.1364/OL.42.003048.

[23] Ó. Pérez-Benito, R. Weigand, Nano-dispersion-scan: measurement of sub-7-fs laser pulses using second-harmonic nanoparticles, Opt. Lett. 44 (20) (2019) 4921–4924, http://dx.doi.org/10.1364/OL.44.004921.

[24] I. Sytcevich, C. Guo, S. Mikaelsson, J. Vogelsang, A.-L. Viotti, B. Alonso, R. Romero, P.T. Guerreiro, I.J. Sola, A. L'Huillier, H. Crespo, M. Miranda, C.L. Arnold, Characterizing ultrashort laser pulses with second harmonic dispersion scans, J. Opt. Soc. Am. B 38 (5) (2021) 1546–1555, http://dx.doi.org/10.1364/JOSAB.412535.